

## Ultrafast Tunable Broadband Optical Anisotropy in Two-Dimensional ReS<sub>2</sub>

Sung Bok Seo,<sup>1,†</sup> Sanghee Nah<sup>2,†</sup> Muhammad Sajjad<sup>3,†</sup> Nirpendra Singh,<sup>3,4</sup> Youngwook Shin,<sup>5,6</sup> Younghyun Kim,<sup>5,6</sup> Jaekyun Kim,<sup>5,6</sup> and Sangwan Sim<sup>1,\*</sup>

<sup>1</sup>*Division of Electrical Engineering, Hanyang University, Ansan, 15588, Korea*


<sup>2</sup>*Seoul Center, Korea Basic Science Institute (KBSI), Seoul 02841, Korea*

<sup>3</sup>*Department of Physics, Khalifa University of Science and Technology, Abu Dhabi 127788, United Arab Emirates*

<sup>4</sup>*Center for Catalysis and Separation (CeCaS), Khalifa University of Science and Technology, Abu Dhabi 127788, United Arab Emirates*

<sup>5</sup>*Department of Photonics and Nanoelectronics, Hanyang University, Ansan 15888, Korea*

<sup>6</sup>*BK21 FOUR ERICA-ACE Center, Hanyang University, Ansan, Gyeonggi 15588, Korea*

 (Received 30 November 2021; revised 25 May 2022; accepted 8 June 2022; published 6 July 2022)

Anisotropic two-dimensional materials provide promising platforms for polarization-driven optoelectronic and photonic devices. In particular, layered rhenium disulfide (ReS<sub>2</sub>) has recently attracted intensive attention due to its unique linear dichroism. However, control over the optical properties of ReS<sub>2</sub> is mostly limited to the band-edge excitons, which significantly limits the application wavelength range. Here, we utilize ultrafast transient absorption microscopy to tune the broadband optical anisotropy of few-layer ReS<sub>2</sub>. We observe a broad nonexcitonic photoinduced-absorption feature, which exhibits weak anisotropy immediately after pump excitation, but, surprisingly, shows a strong polarization dependence after a few picoseconds, leading to a broadband enhancement in the optical anisotropy. We attribute this to carrier cooling and subsequent anisotropic free-carrier absorption due to anisotropic carrier effective masses. This work provides not only a principle for the ultrafast active control of broadband polarization-sensitive photonic devices but also insights into anisotropic carrier dynamics in two-dimensional materials.

DOI: [10.1103/PhysRevApplied.18.014010](https://doi.org/10.1103/PhysRevApplied.18.014010)

### I. INTRODUCTION

Two-dimensional (2D) transition-metal dichalcogenides (TMDs), often represented by  $MX_2$  ( $M = \text{W}$  and  $\text{Mo}$ ;  $X = \text{Se}$  and  $\text{S}$ ), provide excellent optical and optoelectronic properties, such as a thickness-engineered electronic band-gap nature, stable excitons, and valley selectivity [1–5]. As a rising member of the 2D TMDs, rhenium disulfide (ReS<sub>2</sub>) offers unique light-matter interaction properties that  $MX_2$  materials do not exhibit [6–8]. Due to relatively low in-plane crystal symmetry in ReS<sub>2</sub>, chains of rhenium atoms are aligned along a specific crystal direction ( $b$  axis), making light-matter interactions strongly dependent on light-polarization orientation [9–11]. This optical anisotropy enables various optoelectronic applications, such as highly sensitive polarization detectors [12–14], polarized-light emitters [15], saturable absorbers [16,17], and light-polarization-controlled ultrafast optical switches [18–20]. ReS<sub>2</sub> possesses additional application advantages over other 2D materials. First, while the circular-polarization-selective valley-exciton

transitions in  $MX_2$  are possible only for ultrathin odd layer numbers [3–5], the linear-polarization selectivity in ReS<sub>2</sub> is available for all layer numbers [9–11]. Second, the air stability of ReS<sub>2</sub> is excellent [8], unlike exfoliated black phosphorus, another representative 2D material with optical anisotropy, which degrades rapidly upon air exposure [21].

However, the optical anisotropy in ReS<sub>2</sub> is still not fully exploited. This is because modulation of the anisotropic characteristics in ReS<sub>2</sub> has been mostly limited to the band-edge excitons [18–20,22–24], although its intrinsic optical anisotropy persists over a wide range from near-infrared to ultraviolet [25,26]. One example is the recently reported optical Stark effect [18,19], which can be utilized to control anisotropic excitons in ReS<sub>2</sub> selectively, but the available wavelength range is inherently confined to the narrow spectral window near the band-edge excitons. Several recent optical pump-probe studies observed polarization-dependent modulation in transmittance and reflectance by laser-pulse injection [20,22–24], but the probing wavelength has been mostly confined to the narrow region near excitons as well, and a method to enhance the intrinsic anisotropy of ReS<sub>2</sub> has not been studied. Thus, control of the optical anisotropy in ReS<sub>2</sub> is still poorly explored, preventing the development of

\*swsim@hanyang.ac.kr

†These authors contributed equally to this work.

ReS<sub>2</sub>-based devices capable of actively switching the broadband polarization sensitivity. We note that important studies have been reported on the optical anisotropy of ReS<sub>2</sub>, which varies depending on the number of layers [11,27–32] and stacking order [33,34]. These are not directly correlated with active control of the anisotropy.

Here, we modulate the optical anisotropy of few-layer ReS<sub>2</sub> over a broad wavelength range of 500–950 nm by laser-pulse injection. Ultrafast broadband transient absorption microscopy is utilized to monitor picosecond changes in the degree of linear polarization in the absorption profile. We observe a nonexcitonic broad photoinduced-absorption feature, which exhibits no polarization dependence immediately after pump excitation, but shows a strong anisotropy after about 1.5 ps. Consequently, the anisotropic photoinduced absorption increases the linear polarization degree of the absorption. We find that this modulation effect originates from anisotropic free-carrier absorption due to intrinsic anisotropy in the carrier effective mass in ReS<sub>2</sub>. This work provides a principle for the switching of optical anisotropy based on anisotropic free-carrier absorption, which can be utilized for polarization-sensitive optoelectronic devices. Additionally, this work offers an insight into the anisotropic ultrafast carrier dynamics of 2D materials.

## II. METHODS

### A. Sample preparation

The ReS<sub>2</sub> flake on a sapphire substrate is prepared by mechanical exfoliation from commercially available bulk crystals.

### B. Ultrafast broadband transient absorption microscopy

We use a Yb:KGW femtosecond amplifier system (Light Conversion, PHAROS), generating laser pulses at 400 kHz with a pulse duration of 230 fs, to produce the pump and probe beams. One portion of the amplifier output is directed to a noncollinear optical parametric amplifier (Light Conversion, ORPHEUS-N) to generate 30-fs pump pulses centered at 1.55 eV. Focusing the pump beam onto a beta-barium borate crystal tunes the energy to 3.1 eV. The pump beam is spectrally filtered with a short-pass filter blocking the 1.55 eV pulses and modulated with an optical chopper at 125 Hz. Another portion of the amplifier is focused onto a YAG crystal to generate a white-light supercontinuum probe beam. The probe beam passes through a filter, cutting off the fundamental beam, and is bounced off between two negatively chirped mirrors several times to compensate for positive group-velocity dispersions. The pump and probe beams are combined using a dichroic beam splitter. The collinearly propagating beams are focused onto a sample with a

reflective objective (NA 0.65) and transmitted beams are collected with an objective (NA 0.7). Only the probe beam is guided to a monochromator, and spectrally dispersed photons are detected using an electron-multiplying charge-coupled-device camera triggered at 250 Hz. The changes in the probe absorption with sequential pump-on ( $A_{\text{pump}}$ ) and pump-off ( $A_0$ ) events are recorded at different pump-probe time delays controlled with a motorized linear stage. The pump and probe intensities are modulated with neutral density filters, and the polarization is controlled with broadband half-wave plates in the pump and probe paths. Data acquisition is carried out with home-built LabView software.

## III. RESULTS AND DISCUSSION

Figure 1(a) displays an optical image of the few-layer ReS<sub>2</sub> sample on a sapphire substrate prepared by the mechanical exfoliation method. Bonding between Re atoms is relatively strong, thereby forming Re-Re chains along the direction of the  $b$  axis of the crystal. Thus, ReS<sub>2</sub> flakes are usually cleaved along it [27], as identified in the optical image [yellow line, Fig. 1(a)]. This is further confirmed by optical spectroscopy, as discussed later. The flake thickness measured by atomic force microscopy is about 4.5 nm, corresponding to 6 layers [11]. We present the electronic band structure of ReS<sub>2</sub> and complex dielectric functions in the Appendix.

First, we explore the steady-state optical anisotropy of ReS<sub>2</sub> through polarization-dependent absorption. The incident light is linearly polarized, and its polarization angle is defined as the relative angle between orientations of the polarization and the  $b$  axis [see Fig. 1(a)]. Figures 1(b) and 1(c) display measured full absorbance spectra and corresponding line-cut profiles at several different energies, respectively. The absorption profile is modulated with a period of 180° by the polarization angle of light. In particular, the intensity of the overall absorption is the strongest (weakest) for polarization parallel (perpendicular) to the  $b$  axis, which is in agreement with previous studies [12,35]. This result suggests that comparing absorption spectra for the two polarization angles (i.e., parallel and perpendicular to the  $b$  axis) will be a reasonable way to discuss the broadband anisotropy of ReS<sub>2</sub>. In this sense, we define the linear polarization degree of the absorption as

$$\rho = \frac{A_{\parallel} - A_{\perp}}{A_{\parallel} + A_{\perp}}. \quad (1)$$

The spectra for  $A_{\parallel}$  and  $A_{\perp}$  are shown in Fig. 1(d), where  $A_{\parallel}$  is higher than  $A_{\perp}$  over our entire spectral window. Thus,  $\rho$  in Fig. 1(e) shows only a positive sign.

We identify several absorption peaks. First, two anisotropic excitons, Ex<sub>1</sub> and Ex<sub>2</sub>, are observed at 1.49 and 1.51 eV, respectively, as indicated by the magenta and

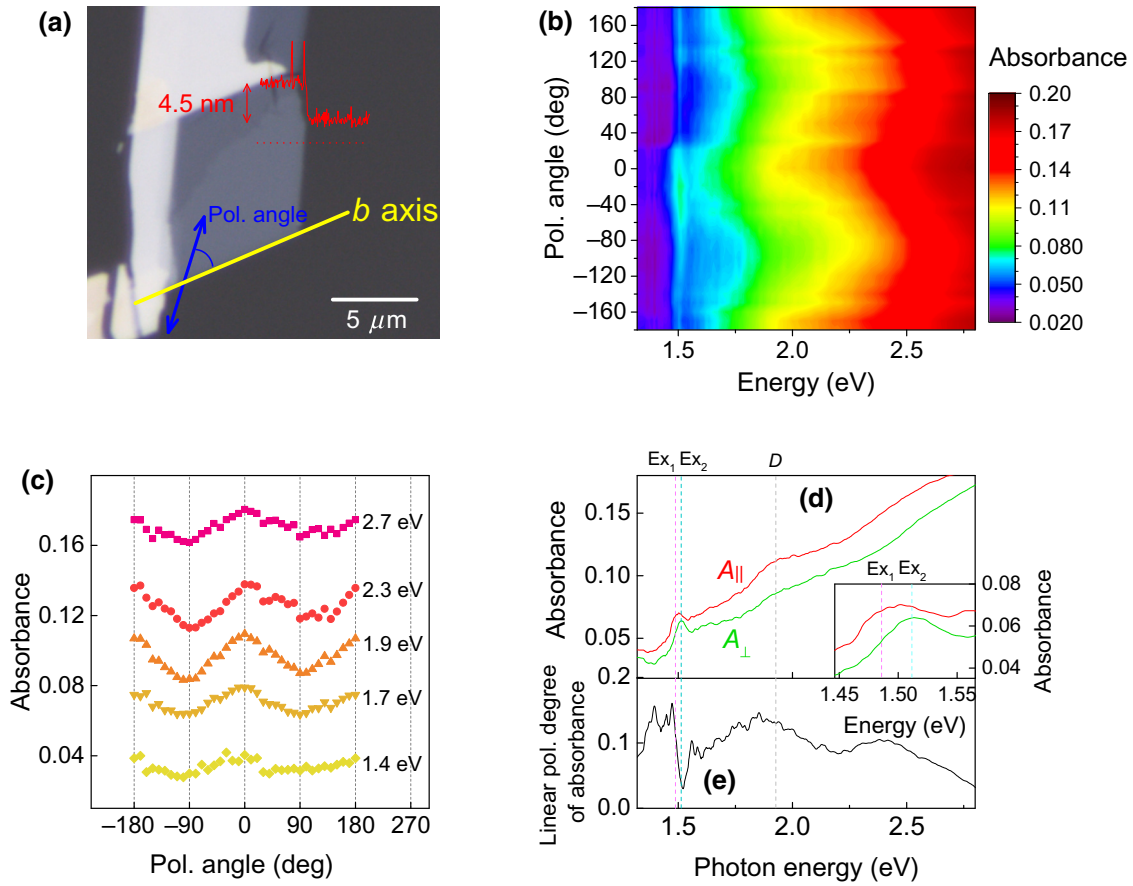


FIG. 1. Steady-state characterization. (a) Optical image of a 6-layer  $\text{ReS}_2$  sample. Corresponding height profile is shown by the red graph. Blue arrow represents the polarization orientation of light. Polarization angle of light is measured relative to the crystal's  $b$  axis, as denoted by the yellow line. Polarization-dependent absorbance (b) and corresponding line-cut profiles at several different photon energies (c). (d) Absorbance spectra for light-polarization parallel (red) and perpendicular (green) to the  $b$  axis. Vertical dashed lines indicate the anisotropic absorption resonance energies for  $\text{Ex}_1$  (magenta),  $\text{Ex}_2$  (cyan), and  $D$  (gray), respectively. Inset is a magnified view near  $\text{Ex}_1$  and  $\text{Ex}_2$ . (e) Linear polarization degree of the absorbance obtained from the absorbance spectra in (d).

green dashed lines in Fig. 1(d) and the magnified view (inset). Spectral weights of these anisotropic excitons are maximized when the polarization angle is  $15^\circ$  for  $\text{Ex}_1$  and  $88^\circ$  for  $\text{Ex}_2$  (Fig. S1 within the Supplemental Material [36]) [11,18,37]. Thus,  $\text{Ex}_1$  ( $\text{Ex}_2$ ) shows a stronger response with  $\parallel$  ( $\perp$ ) polarization, as displayed in the inset of Fig. 1(d). Due to  $\text{Ex}_2$ , the linear polarization degree of the absorption in Fig. 1(e) exhibits a local minimum near 1.51 eV. We also observe a high-energy anisotropic peak at 1.92 eV, as indicated by the gray dashed line in Fig. 1(d), the spectral weight of which is maximized at  $\parallel$  polarization (Fig. S1 within the Supplemental Material [36]). This anisotropic resonance, due to the transition from Re  $5d$ -S  $3p$  bonding to Re  $5d$ -S  $3p$  antibonding, was identified by Ho *et al.* in bulk  $\text{ReS}_2$  [25]. Following Ref. [25], we denote this resonance as  $D$ .

Now we modulate the anisotropic absorption of  $\text{ReS}_2$  through optical pulse injection. Ultrafast optical-pump–white-light-probe microscopy monitors the pump-induced

change in absorbance,  $\Delta A = A_{\text{pump}} - A_0$ , as a function of pump-probe time delay ( $t$ ), where  $A_{\text{pump}}$  ( $A_0$ ) is the absorbance with (without) the pump [Fig. 2(a); see Sec. II]. The pump fluence is fixed to  $0.8 \text{ mJ cm}^{-2}$ . We perform probe-polarization-dependent measurements to identify changes in the optical anisotropy. Polarization of the pump is fixed at  $45^\circ$  relative to the  $b$  axis because the absorption anisotropy is weak at a pump energy of 3.1 eV. Actually, we observe no significant pump-polarization dependence of  $\Delta A$  (Fig. S2 within the Supplemental Material [36]). Figures 2(b) and 2(c) display 2D contour plots of  $\Delta A$  measured for probe polarization parallel and perpendicular to the  $b$  axis, denoted as  $\Delta A_{\parallel}$  and  $\Delta A_{\perp}$ , respectively. There, blue-colored negative signals correspond to photoinduced bleaching (PB). While we observe PB at  $\text{Ex}_1$  and  $D$  resonances in  $\Delta A_{\parallel}$  [Fig. 2(b)], PB in  $\Delta A_{\perp}$  is seen at the  $\text{Ex}_2$  energy [Fig. 2(c)]. The energy positions of the PB and their polarization dependence agree with the steady-state response in Fig. 1(d). In Figs. 2(b) and 2(c),

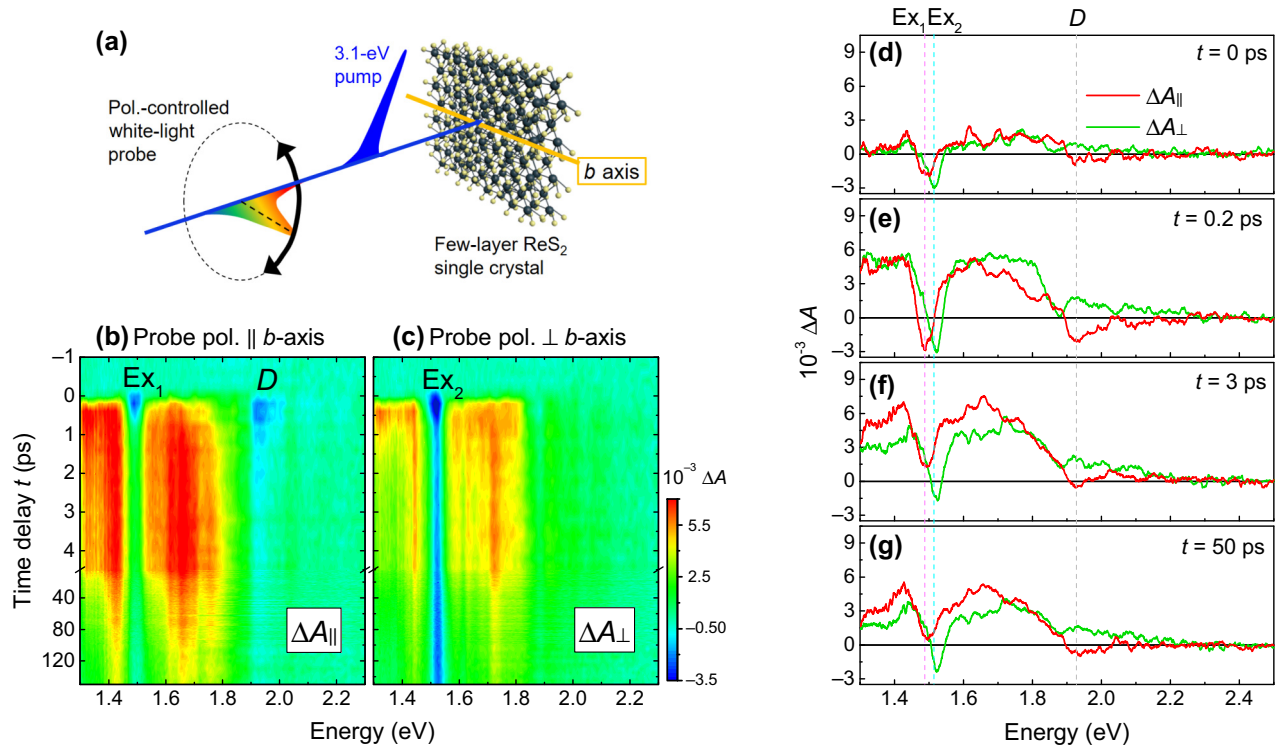


FIG. 2. Pump-induced transient absorption dynamics. (a) Schematic description of the optical-pump–white-light-probe experiment. (b), (c) Time- and spectrally resolved differential absorbance for probe polarization parallel (b) and perpendicular (c) to the  $b$  axis, denoted as  $\Delta A_{\parallel}$  and  $\Delta A_{\perp}$ , respectively. (d)–(g) Corresponding transient spectra for  $\Delta A_{\parallel}$  (red) and  $\Delta A_{\perp}$  (green) are shown at several different pump-probe time delays. Vertical dashed lines indicate energies for  $Ex_1$  (magenta),  $Ex_2$  (cyan), and  $D$  (gray).

the red-colored positive signals observed over the broad range of 1.3–1.7 eV indicate photoinduced absorption (PA). Importantly, the intensity of PA in  $\Delta A_{\parallel}$  is remarkably stronger than that in  $\Delta A_{\perp}$ , leading to an increase in the degree of linear polarization,  $\rho$  [Eq. (1)]. This is because its pump-induced change ( $\Delta\rho$ ) is approximately proportional to the difference between  $\Delta A_{\parallel}$  and  $\Delta A_{\perp}$ , that is

$$\Delta\rho = \rho_{\text{pump}} - \rho_0 \propto \Delta A_{\parallel} - \Delta A_{\perp}, \quad (2)$$

where  $\rho_{\text{pump}}$  ( $\rho_0$ ) denotes the linear polarization degree of the absorption with (without) pump (see Sec. 1 within the Supplemental Material for more details [36]). Thus, the anisotropic PA enhances the absorption anisotropy.

Next, we compare the transient  $\Delta A_{\parallel}$  and  $\Delta A_{\perp}$  spectra at several different time delays [Figs. 2(d)–2(g)]. We observe spectral dips at  $Ex_1$  and  $Ex_2$  energies (indicated by magenta and green dashed lines), which originate from exciton bleaching due to state filling and screened Coulomb interactions by excited carriers. Detailed dynamics of exciton bleaching in  $\text{ReS}_2$  have been intensively studied elsewhere [22,23,38,39]. Bleaching of the  $D$  peak is well identified in  $\Delta A_{\parallel}$  (cyan dashed line), but not in  $\Delta A_{\perp}$ , confirming the anisotropy of this transition. However, rather than these anisotropic peaks, we focus on the broad PA signals that play a key role in modulating the

optical anisotropy. As shown in Figs. 2(d) and 2(e), the overall heights of PA in  $\Delta A_{\parallel}$  and  $\Delta A_{\perp}$  are similar at early time delays,  $t=0$  and 0.2 ps. This response is not helpful for anisotropy modulation, as outlined by Eq. (2). However, at longer time delays [ $t=3$  and 50 ps; Figs. 2(f) and 2(g)], the broad PA in  $\Delta A_{\parallel}$  is significantly larger than that in  $\Delta A_{\perp}$ , which can lead to significant modulation of the absorption anisotropy. Also, the bleaching of  $Ex_1$  in  $\Delta A_{\parallel}$  is completely buried in the strong PA, so the sign of  $\Delta A_{\parallel}$  is positive for all energies below the  $D$  peak, suggesting the nonexcitonic origin of the broad PA feature. Later, we discuss possible physical mechanisms. We can see some spikelike peaks at 1.6–1.7 eV, probably originating from a series of excitons lying above  $Ex_2$  [40]. Given that exciton bleaching causes negative  $\Delta A_{\parallel}$ , this feature can be interpreted as small exciton responses superimposed on the large positive PA band with a positive sign.

To confirm the anisotropy of PA, we measure  $\Delta A$  spectra while continuously rotating the probe polarization at  $t=3$  ps. In Fig. 3(a), the red-colored PA bands are maximized (minimized) at  $\parallel$  ( $\perp$ ) polarization, which is also well shown by the corresponding polar plot in Fig. 3(b). This result further justifies the use of the linear polarization degree of the absorption based on the two polarizations,  $\parallel$  and  $\perp$ . The observed polarization dependence phenomenologically agrees with recently

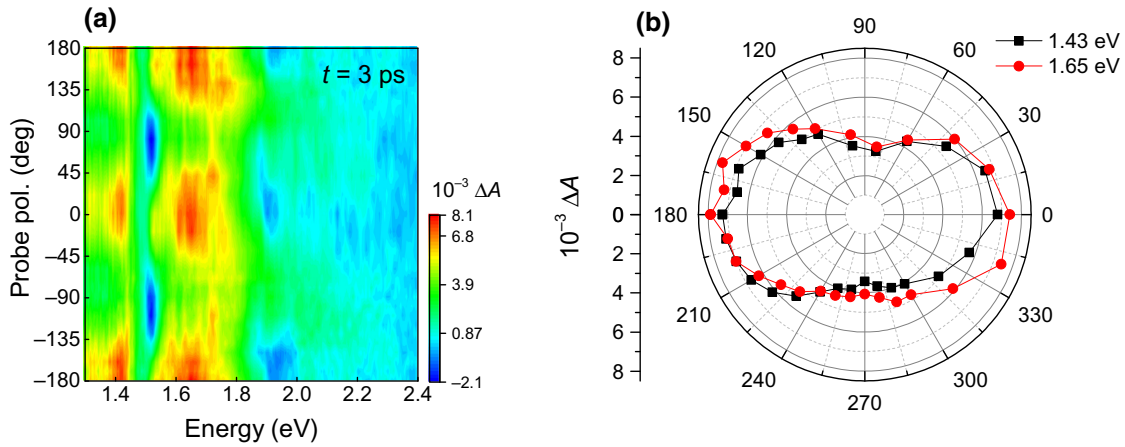


FIG. 3. Anisotropic photoinduced absorption. (a) Transient differential absorption measured while rotating the probe polarization. Pump-probe time delay is fixed at  $t = 3$  ps. (b) Corresponding polar plot at two different photon energies exhibiting photoinduced absorption.

reported intensity-scan measurements on  $\text{ReS}_2$ , where the anisotropic nonlinear optical effect is the strongest at  $\parallel$  polarization due to the large excited-state absorption [17].

Now, we investigate how the optical pulse injection modulates the absorption anisotropy. We obtain the pump-modulated linear polarization degree of the absorption from the measured steady state [ $A_{\parallel}$  and  $A_{\perp}$ ; Fig. 1(d)] and differential absorbance [ $\Delta A_{\parallel}$  and  $\Delta A_{\perp}$ ; Figs. 2(b) and 2(c)]. Figure 4(a) displays the result at  $t = 3$  ps ( $\rho_{\text{pump}}$ ; red line) with the nonmodulated one ( $\rho_0$ ; black line).  $\rho_{\text{pump}}$  is larger than  $\rho_0$  at about 1.3–1.7 eV, indicating

enhancement of anisotropy. To see this more clearly, we plot  $\Delta\rho = \rho_{\text{pump}} - \rho_0$  in Fig. 4(b), where a positive sign is observed at 1.3–1.7 eV, except at the  $\text{Ex}_1$  resonance (magenta dashed line). This negative dip arises because bleaching of  $\text{Ex}_1$  leads to a small amplitude of  $\Delta A_{\parallel}$  [Figs. 2(f) and 2(g)], which hinders the increase of  $A_{\parallel}$ . For a similar reason, negative  $\Delta\rho$  at the  $D$  resonance (gray dashed line) is observed due to a pump-induced decrease in the linear polarization degree of the absorption. Therefore, pump injection rather weakens the anisotropy of  $\text{Ex}_1$  and  $D$  resonances that exhibit strong absorption at

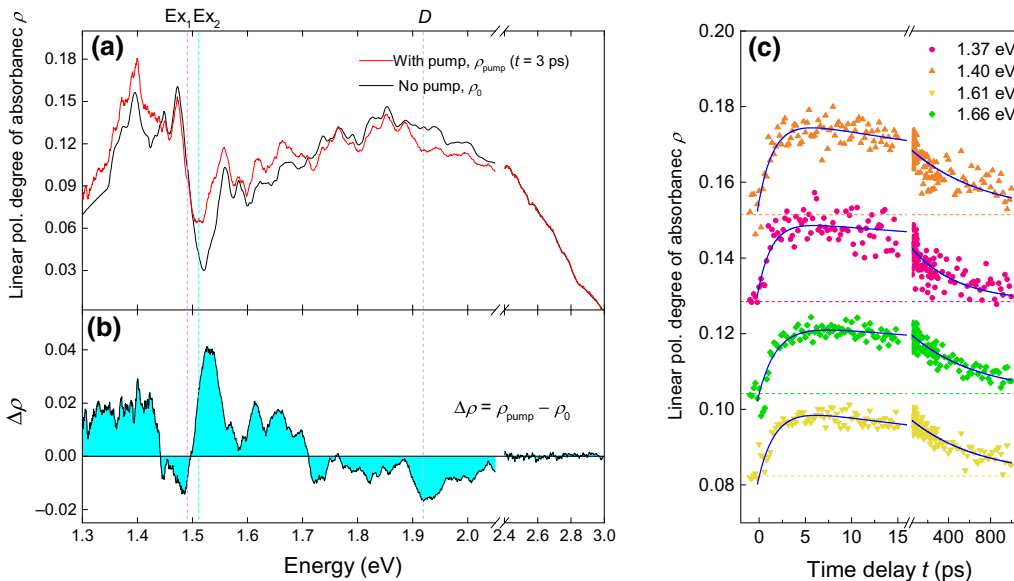


FIG. 4. Modulation of anisotropy. (a) Pump-modulated linear polarization degree of the absorbance at  $t = 3$  ps (red line). Nonmodulated one [Fig. 1(e)] is shown for comparison (black line). Vertical dashed lines indicate energies for  $\text{Ex}_1$  (magenta),  $\text{Ex}_2$  (cyan), and  $D$  (gray). (b) Difference between the two graphs presented in (a). (c) Dynamics of the linear polarization degree of the absorbance at several probe energies, showing increased anisotropy. Horizontal dashed lines are corresponding nonmodulated values. Blue lines are exponential fits.

$\parallel$  polarization, although it raises anisotropy in the nonexcitonic region below 1.7 eV. Note that the overall amplitude of  $\Delta\rho$  is scaled along with pump fluence, but the spectral shape does not change significantly (Fig. S3 within the Supplemental Material [36]).

We next proceed by investigating the time dependence of anisotropy modulation. Figure 4(c) shows the dynamics of  $\rho_{\text{pump}}$  at several energies exhibiting positive  $\Delta\rho$ . All the traces reach their maximum at around  $t=3$  ps, and a corresponding rise-time constant of  $(1.7 \pm 0.2)$  ps is obtained from exponential fitting (blue lines). The  $\rho_{\text{pump}}$  traces return to their nonmodulated values (dashed lines) with decay-time constants of  $(350 \pm 150)$  ps. The obtained time constants determine the speed of anisotropy modulation. We discuss the origins of these time constants at the end of this section.

Now, we explore the possible origins of anisotropy modulation. As discussed above, the pump-enhanced anisotropy arises from the polarization-dependent PA, which exhibits a larger amplitude at  $\parallel$  polarization than that at  $\perp$  polarization [e.g., Fig. 2(f)]. Thus, it is instructive to understand PA first. The representative causes of PA in semiconductors are as follows: lattice heating, band-gap renormalization (BGR), and free-carrier absorption (FCA). The first mechanism, lattice heating, results from the transfer of excess energy formed in the electronic system by the absorbed pump photons to the lattice system through electron-phonon coupling. It has been recently found that the  $E_g$ -like in-plane phonon mode (labeled as  $L_3$ ) at about  $151 \text{ cm}^{-1}$  exhibits strong interactions with electrons in  $\text{ReS}_2$  [41]. Such interactions transfer the high energy of carriers created by the pump to the lattice, which raises the lattice temperature. In  $\text{ReS}_2$ , an increase in the lattice temperature shrinks the optical band gap, leading to an increase in the absorption near the optical absorption edge [42]. However, in our experiment, the estimated amounts of optical band-gap shrinkage due to lattice heating are similar for  $\parallel$  and  $\perp$  polarizations (see the Supplemental Material, Sec. 2 [36,43]), which cannot explain the observed large difference of PA between  $\Delta A_{\parallel}$  and  $\Delta A_{\perp}$ . Also, in 2D TMDs, including  $\text{ReS}_2$ , the lattice-heating effect has a meaningful effect on the transient absorption signal about 10 ps after the pump [39,44], but this time delay is far later than the observed rise time of anisotropy modulation, about 1.7 ps [Fig. 4(b)]. Thus, we exclude the lattice-heating effect as an explanation for the observed anisotropic PA response. The second mechanism is BGR, which describes a reduction of the band gap due to many-body interactions of pump-excited-electron and -hole plasmas. The BGR effect sublinearly depends on the excited carrier density [45], whereas the measured peak  $\Delta A$  exhibits a linear dependence [Fig. 5(a)]. Also, BGR redshifts the overall absorption spectrum [46,47], but the shape of the  $\Delta A$  expected thereof deviates far from the observed one (Fig. S4 within the Supplemental Material

[36]). These results suggest that BGR is not the dominant factor for PA. The third mechanism is FCA. In this process, the corresponding PA signal depends linearly on the pump-excited carrier density, agreeing with our observation [Fig. 5(a)]. We note that pump-created excitons can also absorb probe photons. However, because the density of pump-excited electron-hole pairs ( $\sim 10^{13}\text{--}10^{14} \text{ cm}^{-2}$ ) is above the Mott threshold ( $10^{12}\text{--}10^{13} \text{ cm}^{-2}$ ) [48,49], most of the excitons are expected to be ionized. Thus, we attribute the observed PA to FCA. This attribution agrees with recently reported near-IR FCA in a  $\text{ReS}_2$  thin film [50].

Here, we discuss FCA in more detail. There are two well-known types of FCA: the Drude-type and the inverse bremsstrahlung-type FCA [51,52]. In the first type of process, carrier-carrier scattering provides additional momentum for satisfying energy-momentum conservation. Since this Drude-type FCA is usually observed below the plasma frequency, terahertz [53,54] or mid-infrared [55] spectroscopy is commonly used to detect it. On the other hand, in the second type of process, FCA is assisted by scattering between carriers and ions (e.g., photoionized ions or ionized impurities) and can emerge in the spectral region above the plasma frequency [51]. In our experiment, the probe window (1.3–3 eV) is far above the estimated plasma frequency ( $\sim 0.58$  eV); thus, the inverse bremsstrahlung-type FCA is expected. The associated FCA coefficient ( $\alpha_{\text{FCA}}$ ) of this FCA mechanism is inversely related to the carrier effective mass ( $m^*$ ),  $\alpha_{\text{FCA}} \propto (m^*)^{-3/2}$  (Sec. 3 within the Supplemental Material [36,56,57]). Near the conduction-band edge in  $\text{ReS}_2$ , the ratio between the electron effective mass in the direction of the  $b$  axis ( $m_{\parallel}^*$ ) and that in the perpendicular direction ( $m_{\perp}^*$ ) is about  $m_{\parallel}^*:m_{\perp}^*=0.56:0.98$  [58]. The corresponding ratio of  $\alpha_{\text{FCA}}$  is  $(m_{\parallel}^*)^{-3/2}:(m_{\perp}^*)^{-3/2} \sim 2.3:1$ . Similarly, the  $\alpha_{\text{FCA}}$  ratio obtained from hole effective masses ( $m_{\parallel}^*:m_{\perp}^*=1.6:2.2$ ) [59] near the valence-band edge is about 1.6:1. Both results roughly agree with the observed ratio of  $\Delta A_{\parallel}$  to  $\Delta A_{\perp}$  ( $\sim 1.9:1$ ) in Fig. 3(b). Therefore, we attribute the large FCA at  $\parallel$  polarization to the smaller carrier effective mass in that orientation.

Additionally, we estimate the relative contribution ratio of electrons and holes to  $\alpha_{\text{FCA}}$ . In the direction of the  $b$  axis, the effective electron and hole masses are  $m_e^*=0.56 m_0$  and  $m_h^*=1.6 m_0$ , respectively, where  $m_0$  is the free-electron mass [58]. Thus, the corresponding  $\alpha_{\text{FCA}}$  ratio is  $(m_e^*)^{-3/2}:(m_h^*)^{-3/2} = 4.8:1$ . Similarly, the  $\alpha_{\text{FCA}}$  ratio in the direction perpendicular to the  $b$  axis is estimated to be  $(m_e^*)^{-3/2}:(m_h^*)^{-3/2} = 3.4:1$  [58]. These estimations show that electrons make a larger contribution to the FCA signal at both  $\parallel$  and  $\perp$  polarizations.

We need to consider the steady-state anisotropy of the absorption edge. It is known that the indirect absorption edge below  $\text{Ex}_1$  exhibits a stronger response at  $\parallel$  polarization than that measured at  $\perp$  polarization [60].

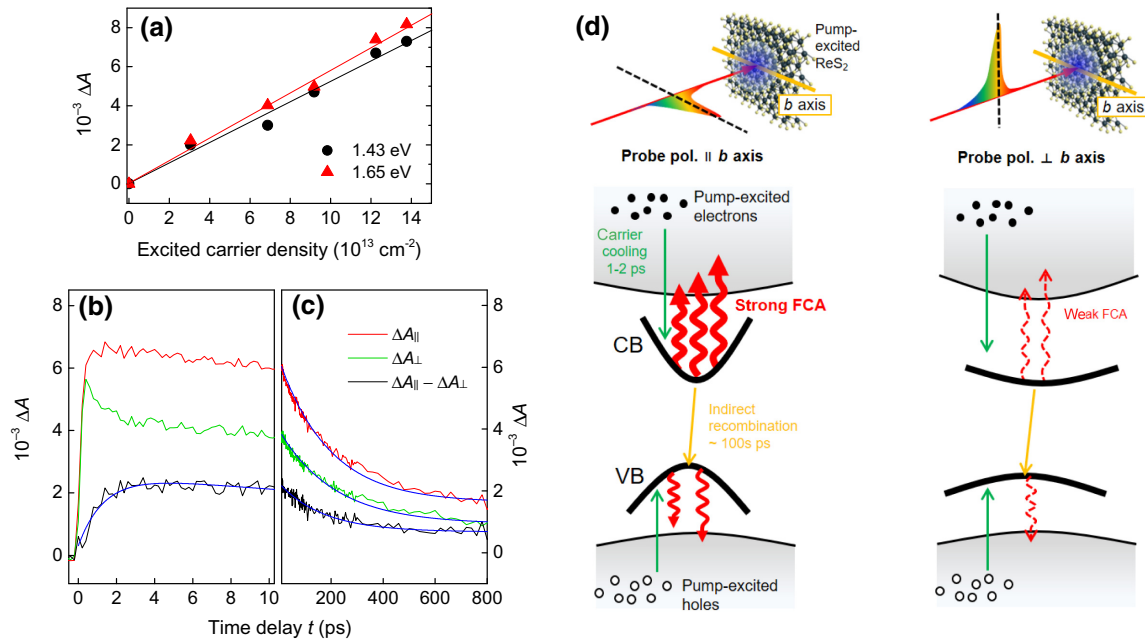


FIG. 5. Origin of anisotropic photoinduced absorption. (a) Differential absorbance at  $t=3$  ps for  $\Delta A_{\parallel}$  is shown as a function of excited carrier density. Solid lines are guides for the eye. (b),(c) Dynamics of differential absorbance,  $\Delta A_{\parallel}$  (red) and  $\Delta A_{\perp}$  (green), and their difference ( $\Delta A_{\parallel} - \Delta A_{\perp}$ ; black) measured at 1.43 eV are shown with exponential fits (blue smooth lines). (d) Schematic summary of polarization-dependent photoinduced absorption. Left and right panels describe the carrier dynamics measured for probe polarization parallel and perpendicular to the  $b$  axis, respectively. Filled (open) circles represent pump-generated electrons (holes). For both polarizations, pump-excited carriers are cooled to the band edge on a timescale of 1–2 ps (green arrows). Observed photoinduced absorption band is due to absorption of probe photons by the free carriers, i.e., FCA (red wavy arrows). FCA for probe polarization parallel to the  $b$  axis (left panel) is stronger than that measured for probe polarization perpendicular to the  $b$  axis (right panel), resulting from the fact that the FCA coefficient is inversely related to the carrier effective mass. Left (right) panel depicts a smaller (larger) carrier effective mass due to a larger (smaller) band curvature at the band edge. For both polarizations, carriers vanish by indirect recombination on a timescale of about 100 ps (orange arrows). CB and VB represent the conduction and valence band, respectively.

Thus, one can expect that this anisotropic steady-state response may affect the transient anisotropic  $\Delta A$  discussed so far. Under optical excitation, the absorption edge generally undergoes shifts and bleaching [61]. The former is caused by lattice heating and BGR, neither of which are adequate to explain the observed PA, as discussed above. The latter, caused by band filling, may exhibit relatively large photoinduced modulation due to its intrinsic anisotropy. However, the corresponding sign of  $\Delta A$  should be negative, opposite to the observation. Thus, it is hard to expect that the bleaching of the absorption edge will directly affect the observed anisotropic PA response.

Finally, we discuss the dynamics of FCA. Figure 5(b) shows PA dynamics at an early time delay measured at 1.43 eV (similar results are obtained at other energies; see Fig. S5 within the Supplemental Material [36]). We can see that  $\Delta A_{\perp}$  (green) shows a picosecond fast decay component absent in  $\Delta A_{\parallel}$  (red). Consequently, their difference,  $\Delta A_{\parallel} - \Delta A_{\perp}$  (black line), grows with a relatively slow rise-time constant of about 1.5 ps. This causes the retarded rise of anisotropy modulation in Fig. 4(c) because  $\Delta\rho \propto \Delta A_{\parallel} - \Delta A_{\perp}$  [Eq. (2)]. In the above paragraph, we attribute the polarization-dependent FCA to the

carrier effective mass that varies with orientation, which is determined by band curvatures at the band edge. However, immediately after absorbing pump photons, a large portion of carriers stay at higher-energy states than the band edge because the pumping energy (3.1 eV) is much larger than the quasiparticle band gap ( $\sim 1.6$  eV) [26]. Hence, the orientation-dependent carrier effective mass can affect FCA *after* most of the carriers are cooled to the band edge. The carrier cooling time in 2D TMDs is about 1.5 ps [48], which agrees well with the rise time of  $\Delta A_{\parallel} - \Delta A_{\perp}$  [black line in Fig. 5(b)]. Therefore, we attribute the rise time of about 1.7 ps for anisotropy modulation [Fig. 4(c)] to the carrier-cooling time. This carrier-cooling process occurs via carrier-phonon coupling, where the  $E_g$ -like in-plane optical phonon mode ( $L_3$ ) plays a key role in ReS<sub>2</sub> [41]. Additionally, we observe reduced rise-time constants of  $\Delta A_{\parallel} - \Delta A_{\perp}$  at low pump fluences (Fig. S6 within the Supplemental Material [36]), consistent with previously reported carrier-cooling behavior in other 2D TMDs [62]. Carrier trapping at defects may contribute to the depopulation of free carriers, but we do not have evidence that this mechanism manifests polarization dependence [22,38]. We rule out Auger

recombination because no pump-fluence dependence of Auger-type processes is observed (Fig. S6 within the Supplemental Material [36]). The long-timescale dynamics of  $\Delta A_{\parallel}$ ,  $\Delta A_{\perp}$ , and their difference exhibit decay-time constants of about  $(230 \pm 50)$  ps due to phonon-mediated indirect recombination [23]. This explains the recovery dynamics of anisotropy modulation in Fig. 4(c). The polarization-dependent free-carrier dynamics discussed so far are summarized in Fig. 5(d) and its caption.

#### IV. APPLICATION OF FREE-CARRIER ABSORPTION

This section discusses the potential applicability of the observed FCA effect. First, we estimate the FCA cross section ( $\sigma_{\text{FCA}}$ ) of few-layer ReS<sub>2</sub> from the observed  $\Delta A$  via the following relationship [63]:

$$\Delta A = \sigma_{\text{FCA}} n, \quad (3)$$

where  $n \approx 1.2 \times 10^{14} \text{ cm}^{-2}$  is the density of pump-generated carriers at a pump fluence of  $0.8 \text{ mJ cm}^{-2}$ . Since the FCA appears as PA in the  $\Delta A$  spectra, the left-hand side of Eq. (3) corresponds to the positive amplitude of the PA band ( $\Delta A \approx 5 \times 10^{-3}$ ) at 1.3–1.7 eV in Fig. 2(e). Thus,  $\sigma_{\text{FCA}}$  is about  $4 \times 10^{17} \text{ cm}^2$  from Eq. (3). Table I compares this  $\sigma_{\text{FCA}}$  value with those in different materials measured at a wavelength range similar to that of our work (730–950 nm). While  $\sigma_{\text{FCA}}$  in few-layer ReS<sub>2</sub> agrees with those in other 2D materials and nanocrystals [64,65], it is orders of magnitude larger than those in bulk materials such as silicon and SnO<sub>2</sub> [65,66]. The large free-carrier effect in nanomaterials is probably due to their relatively small carrier mean scattering times, which are inversely proportional to  $\sigma_{\text{FCA}}$  [65]. Importantly, the large free-carrier effect in nanomaterials provides a potential for photonics applications, such as silicon photonics.

In silicon photonics, heterogeneous integration with various other materials has recently been spotlighted to overcome limited device performance resulting from silicon's intrinsic properties [67,68]. In particular, heterojunctions with 2D materials can enhance the efficiency of light modulation [69–71], enabling a substantial reduction of device size [69–71]. Meanwhile, FCA plays a key role in optical modulation in silicon photonics [72,73]. Especially, FCA is a central mechanism in variable optical attenuators

(VOAs), which are an essential component for controlling optical power levels [73]. However, VOAs generally require a large power consumption due to the low FCA cross section of bare silicon. Thus, there have been various attempts to overcome this challenge via heterogeneous integration with other materials exhibiting larger FCA [68,74]. For example, it has been recently demonstrated that a VOA device including a nanometer-scale-thick heterogeneous layer with a large FCA shows a significantly enhanced light-attenuation performance than that in normal silicon VOAs [73]. This example suggests that the observed strong FCA effect in 2D ReS<sub>2</sub> has potential for the design of high-performance VOA devices in silicon photonics.

FCA is also important for infrared sensing in integrated photonics platforms. In the mid-infrared range, photon energies are much smaller than the band gaps of silicon or germanium such that an interband transition is difficult to use. In contrast,  $\sigma_{\text{FCA}}$  significantly increases with increasing wavelength in the mid-infrared region; thus, heterogeneous integration with high- $\sigma_{\text{FCA}}$  materials can enhance the sensing performance [75]. We therefore expect that the observed FCA in ReS<sub>2</sub> will contribute to polarization-sensitive infrared sensing in integrated photonics platforms.

#### V. CONCLUSION

We modulate the broadband optical anisotropy of few-layer ReS<sub>2</sub> using ultrafast broadband transient absorption microscopy. The optical pump causes a nonexcitonic photoinduced absorption band to arise from free-carrier absorption, which exhibits a significant light-polarization dependence about 1.5 ps after pump excitation. We attribute this to the anisotropic free-carrier absorption after carrier cooling. The anisotropy of free-carrier absorption is due to the intrinsic anisotropy of the carrier effective mass in ReS<sub>2</sub>. Consequently, the degree of linear polarization in the absorption for the wavelength range of 730–950 nm increases, enhancing the broadband optical anisotropy. The modulation principle based on the anisotropic free-carrier absorption found here provides a methodology for the active control of polarization-sensitive photonic devices, such as polarization detectors [12–14], polarized-light emitters [15], transmissive polarizers [76], and lasers operating [16,17] at visible and near-IR wavelengths.

TABLE I. FCA cross section in various materials measured at the wavelength range similar to that of our work (730–950 nm).

Material	Wavelength (nm)	FCA cross section (cm <sup>2</sup> )	References
Few-layer ReS <sub>2</sub>	730–950	$4 \times 10^{-17}$	This work
Few-layer MoS <sub>2</sub>	800	$1 \times 10^{-17} - 2 \times 10^{-17}$	[64]
Si nanocrystals	700–900	$2 \times 10^{-17} - 3 \times 10^{-17}$	[65]
Bulk Si	700–900	$3 \times 10^{-18} - 5 \times 10^{-18}$	[65]
SnO <sub>2</sub>	500–900	$1 \times 10^{-19} - 4 \times 10^{-19}$	[66]



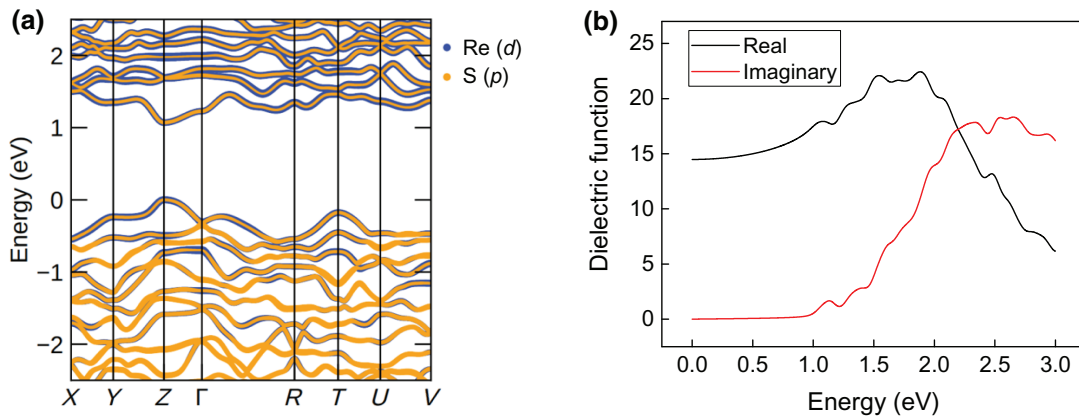


FIG. 6. DFT-calculated orbital-resolved electronic band structure of  $\text{ReS}_2$  (a) and in-plane complex dielectric function (b).

This work also extends the studying range for ultrafast anisotropic phenomena in  $\text{ReS}_2$ , which has, so far, been limited to a narrow spectral region near the excitons. We expect that this work will stimulate similar broadband studies on other anisotropic 2D materials (e.g., black phosphorus,  $\text{ReSe}_2$ ,  $\text{SnSe}_2$ ,  $\text{SnS}$ ,  $\text{WTe}_2$ ,  $\text{ZrTe}_5$ ) and their heterostructures [77–79].

#### ACKNOWLEDGMENTS

S.B.S. and S.S. are supported by the National Research Foundation of Korea (NRF) through the government of Korea (MSIP) (Grant No. NRF-2022R1C1C1003124). This work is, in part, supported by the BK21 FOUR (Fostering Outstanding Universities for Research) funded by the Ministry of Education (MOE, Korea) and National Research Foundation of Korea. The transient absorption experiments are carried out with the Femtosecond Transient Absorption Microscopy (ST015) at the Korea Basic Science Institute (KBSI). S.N. is supported by the KBSI (Project No. C140640) and S.S. is supported by the KBSI under the R&D program (Project No. C030440) supervised by the Ministry of Science and ICT. The absorbance experiment is carried out with an ultrawide wavelength-range microspectrometer system at the Hanyang University ERICA. Y.S. is supported by “the Competency Development Program for Industry Specialists” of the Korean Ministry of Trade, Industry, and Energy (MOTIE), operated by the Korea Institute for Advancement of Technology (KIAT). (Grant No. P0002397, HRD program for Industrial Convergence of Wearable Smart Devices). M.S and N.S acknowledge financial support from the Abu Dhabi Department of Education and Knowledge (ADEK) under Grant No. AARE19-126 and support by the Khalifa University of Science and Technology. This research is supported by the Technology Innovation Program (Grant No. 20015909) through the Korea Evaluation Institute of Industrial Technology (KEIT), funded by the Ministry of Trade, Industry & Energy (MOTIE, Korea).

This research was also supported by KBSI grant funded by Ministry of Education (2021R1A6C101A405).

#### APPENDIX

In this appendix, we present the theoretical calculated electronic band structure [Fig. 6(a)] and complex dielectric function [Fig. 6(b)] of  $\text{ReS}_2$ . The density functional theory (DFT) calculations are performed with the Vienna *ab initio* simulation package [80], using the generalized gradient approximation (Perdew-Burke-Ernzerhof) for the exchange-correlation functional, a cutoff energy of 450 eV, and a  $9 \times 9 \times 9$   $k$  mesh for the non-self-consistent calculations. The van der Waals correction, DFT-D3 [81], is employed, and the spin-orbit coupling is also considered because of heavy Re. Structural optimization is carried out until the Hellmann-Feynman forces drop to  $1 \text{ meV } \text{\AA}^{-1}$  for all atoms.

The overall shape of the calculated structure agrees with previous results [6,26]. Notably, the calculated band gap ( $\sim 1.07$  eV) is smaller than the observed ones [10,42]—as expected for DFT [82]. It is also noteworthy that, although the calculated band structure shows a direct fundamental gap, many conflicting results on the direct or indirect gap nature in  $\text{ReS}_2$  have been reported [26,82,83]. Experimentally, many optical experiments have found that  $\text{ReS}_2$  exhibits indirect-gap characteristics [30,84,85]. These contradictory results on the band-gap nature are an ongoing issue for  $\text{ReS}_2$  [86].

- 
- [1] K. F. Mak, C. Lee, J. Hone, J. Shan, and T. F. Heinz, Atomically Thin  $\text{MoS}_2$ : A New Direct-Gap Semiconductor, *Phys. Rev. Lett.* **105**, 13685 (2010).
  - [2] A. Splendiani, L. Sun, Y. Zhang, T. Li, J. Kim, C. Y. Chim, G. Galli, and F. Wang, Emerging photoluminescence in monolayer  $\text{MoS}_2$ , *Nano Lett.* **10**, 1271 (2010).
  - [3] K. F. Mak, K. He, J. Shan, and T. F. Heinz, Control of valley polarization in monolayer  $\text{MoS}_2$  by optical helicity, *Nat. Nanotechnol.* **7**, 494 (2012).

- [4] H. Zeng, J. Dai, W. Yao, D. Xiao, and X. Cui, Valley polarization in MoS<sub>2</sub> monolayers by optical pumping, *Nat. Nanotechnol.* **7**, 490 (2012).
- [5] X. Xu, W. Yao, D. Xiao, and T. F. Heinz, Spin and pseudospins in layered transition metal dichalcogenides, *Nat. Phys.* **10**, 343 (2014).
- [6] S. Tongay, H. Sahin, C. Ko, A. Luce, W. Fan, K. Liu, J. Zhou, Y. S. Huang, C. H. Ho, J. Yan, *et al.*, Monolayer behaviour in bulk ReS<sub>2</sub> due to electronic and vibrational decoupling, *Nat. Commun.* **5**, 3253 (2014).
- [7] M. Rahman, K. Davey, and S. Z. Qiao, Advent of 2D rhenium disulfide (ReS<sub>2</sub>): Fundamentals to applications, *Adv. Funct. Mater.* **27**, 1606129 (2017).
- [8] X. Li, C. Chen, Y. Yang, Z. Lei, and H. Xu, 2D Re-based transition metal chalcogenides: Progress, challenges, and opportunities, *Adv. Sci.* **7**, 2002320 (2020).
- [9] C. H. Ho, P. C. Liao, Y. S. Huang, and K. K. Tiong, Temperature dependence of energies and broadening parameters of the band-edge excitons of ReS<sub>2</sub> and ReSe<sub>2</sub>, *Phys. Rev. B* **55**, 15608 (1997).
- [10] C. H. Ho, Y. S. Huang, and K. K. Tiong, In-plane anisotropy of the optical and electrical properties of ReS<sub>2</sub> and ReSe<sub>2</sub> layered crystals, *J. Alloys Compd.* **317**, 222 (2001).
- [11] O. B. Aslan, D. A. Chenet, A. M. van der Zande, J. C. Hone, and T. F. Heinz, Linearly polarized excitons in single- and few-layer ReS<sub>2</sub> crystals, *ACS Photonics* **3**, 96 (2016).
- [12] F. Liu, S. Zheng, X. He, A. Chaturvedi, J. He, W. L. Chow, T. R. Mion, X. Wang, J. Zhou, Q. Fu, *et al.*, Highly sensitive detection of polarized light using anisotropic 2D ReS<sub>2</sub>, *Adv. Funct. Mater.* **26**, 1169 (2016).
- [13] E. Zhang, P. Wang, Z. Li, H. Wang, C. Song, C. Huang, Z. G. Chen, L. Yang, K. Zhang, S. Lu, *et al.*, Tunable ambipolar polarization-sensitive photodetectors based on high-anisotropy ReSe<sub>2</sub> nanosheets, *ACS Nano* **10**, 8067 (2016).
- [14] Y. Tang, H. Hao, Y. Kang, Q. Liu, Y. Sui, K. Wei, X. Cheng, and T. Jiang, Distinctive interfacial charge behavior and versatile photoresponse performance in isotropic/anisotropic WS<sub>2</sub>/ReS<sub>2</sub> heterojunctions, *ACS Appl. Mater. Interfaces* **12**, 53475 (2020).
- [15] J. Wang, Y. J. Zhou, D. Xiang, S. J. Ng, K. Watanabe, T. Taniguchi, and G. Eda, Polarized light-emitting diodes based on anisotropic excitons in few-layer ReS<sub>2</sub>, *Adv. Mater.* **32**, 2001890 (2020).
- [16] Y. Cui, F. Lu, and X. Liu, Nonlinear saturable and polarization-induced absorption of rhenium disulfide, *Sci. Rep.* **7**, 40080 (2017).
- [17] X. Meng, Y. Zhou, K. Chen, R. H. Roberts, W. Wu, J. F. Lin, R. T. Chen, X. Xu, and Y. Wang, Anisotropic saturable and excited-state absorption in bulk ReS<sub>2</sub>, *Adv. Opt. Mater.* **6**, 1800137 (2018).
- [18] S. Sim, D. Lee, M. Noh, S. Cha, C. H. Soh, J. H. Sung, M. H. Jo, and H. Choi, Selectively tunable optical Stark effect of anisotropic excitons in atomically thin ReS<sub>2</sub>, *Nat. Commun.* **7**, 13569 (2016).
- [19] S. Sim, D. Lee, J. Lee, H. Bae, M. Noh, S. Cha, M. H. Jo, K. Lee, and H. Choi, Light polarization-controlled conversion of ultrafast coherent-incoherent exciton dynamics in few-layer ReS<sub>2</sub>, *Nano Lett.* **19**, 7464 (2019).
- [20] S. Sim, D. Lee, A. V. Trifonov, T. Kim, S. Cha, J. H. Sung, S. Cho, W. Shim, M. H. Jo, and H. Choi, Ultrafast quantum beats of anisotropic excitons in atomically thin ReS<sub>2</sub>, *Nat. Commun.* **9**, 351 (2018).
- [21] A. Castellanos-Gomez, L. Vicarelli, E. Prada, J. O. Island, K. L. Narasimha-Acharya, S. I. Blanter, D. J. Groenendijk, M. Buscema, G. A. Steele, J. V. Alvarez, *et al.*, Isolation and characterization of few-layer black phosphorus, *2D Mater.* **1**, 025001 (2014).
- [22] Q. Cui, J. He, M. Z. Bellus, M. Mirzokarimov, T. Hofmann, H. Y. Chiu, M. Antonik, D. He, Y. Wang, and H. Zhao, Transient absorption measurements on anisotropic monolayer ReS<sub>2</sub>, *Small* **11**, 5565 (2015).
- [23] X. Wang, K. Shinokita, H. E. Lim, N. B. Mohamed, Y. Miyauchi, N. T. Cuong, S. Okada, and K. Matsuda, Direct and indirect exciton dynamics in few-layered ReS<sub>2</sub> revealed by photoluminescence and pump-probe spectroscopy, *Adv. Funct. Mater.* **29**, 1806169 (2019).
- [24] S. Jiang, J. Yang, Y. Shi, J. Zhao, C. Xie, L. Zhao, J. Fu, P. Yang, Y. Huan, Q. Xie, *et al.*, Salt-assisted growth and ultrafast photocarrier dynamics of large-sized monolayer ReSe<sub>2</sub>, *Nano Res.* **13**, 667 (2020).
- [25] C. H. Ho, P. C. Yen, Y. S. Huang, and K. K. Tiong, Polarized electrolyte-electroreflectance study of ReS<sub>2</sub> and ReSe<sub>2</sub> layered semiconductors, *J. Phys.: Condens. Matter* **13**, 8145 (2001).
- [26] J. P. Echeverry and I. C. Gerber, Theoretical investigations of the anisotropic optical properties of distorted 1T ReS<sub>2</sub> and ReSe<sub>2</sub> monolayers, bilayers, and in the bulk limit, *Phys. Rev. B* **97**, 075123 (2018).
- [27] D. A. Chenet, O. B. Aslan, P. Y. Huang, C. Fan, A. M. van der Zande, T. F. Heinz, and J. C. Hone, In-plane anisotropy in mono- and few-layer ReS<sub>2</sub> probed by Raman spectroscopy and scanning transmission electron microscopy, *Nano Lett.* **15**, 5667 (2015).
- [28] A. Arora, J. Noky, M. Drüppel, B. Jariwala, T. Deilmann, R. Schneider, R. Schmidt, O. Del Pozo-Zamudio, T. Stiehm, A. Bhattacharya, *et al.*, Highly anisotropic in-plane excitons in atomically thin and bulklike 1T'-ReSe<sub>2</sub>, *Nano Lett.* **17**, 3202 (2017).
- [29] J. Jadczyk, J. Kutrowska-Girzycka, T. Smoleński, P. Kosacki, Y. S. Huang, and L. Bryja, Exciton binding energy and hydrogenic Rydberg series in layered ReS<sub>2</sub>, *Sci. Rep.* **9**, 1578 (2019).
- [30] J. M. Urban, M. Baranowski, A. Kuc, Ł Kłopotowski, A. Surrente, Y. Ma, D. Włodarczyk, A. Suchocki, D. Ovchinnikov, T. Heine, *et al.*, Non equilibrium anisotropic excitons in atomically thin ReS<sub>2</sub>, *2D Mater.* **6**, 015012 (2019).
- [31] X. Wang, K. Shinokita, Y. Miyauchi, N. T. Cuong, S. Okada, and K. Matsuda, Experimental evidence of anisotropic and stable charged excitons (trions) in atomically thin 2D ReS<sub>2</sub>, *Adv. Funct. Mater.* **29**, 1905961 (2019).
- [32] R. Gogna, L. Zhang, and H. Deng, Self-hybridized, polarized polaritons in ReS<sub>2</sub> crystals, *ACS Photonics* **7**, 3328 (2020).
- [33] Y. Zhou, N. Maity, A. Rai, R. Juneja, X. Meng, A. Roy, Y. Zhang, X. Xu, J. F. Lin, S. K. Banerjee, *et al.*, Stacking-order-driven optical properties and carrier dynamics in ReS<sub>2</sub>, *Adv. Mater.* **32**, 1908311 (2020).

- [34] Y. Zhou, N. Maity, J. F. Lin, A. K. Singh, and Y. Wang, Nonlinear optical absorption of ReS<sub>2</sub> driven by stacking order, *ACS Photonics* **8**, 405 (2021).
- [35] Y. Y. Wang, J. D. Zhou, J. Jiang, T. T. Yin, Z. X. Yin, Z. Liu, and Z. X. Shen, In-plane optical anisotropy in ReS<sub>2</sub> flakes determined by angle-resolved polarized optical contrast spectroscopy, *Nanoscale* **11**, 20199 (2019).
- [36] See the Supplemental Material at <http://link.aps.org/supplemental/10.1103/PhysRevApplied.18.014010> for polarization-dependent static and transient optical responses, probe energy- and pump-fluence-dependent differential absorbance, and a detailed discussion on the free-carrier absorption and lattice-heating effect.
- [37] C. H. Ho and Z. Z. Liu, Complete-series excitonic dipole emissions in few layer ReS<sub>2</sub> and ReSe<sub>2</sub> observed by polarized photoluminescence spectroscopy, *Nano Energy* **56**, 641 (2019).
- [38] S. Sim, D. Lee, J. Lee, M. Cha, S. Cha, W. Heo, S. Cho, W. Shim, K. Lee, J. Yoo, *et al.*, Role of weak interlayer coupling in ultrafast exciton-exciton annihilation in two-dimensional rhenium dichalcogenides, *Phys. Rev. B* **101**, 174309 (2020).
- [39] S. Sim, H. S. Shin, D. Lee, J. Lee, M. Cha, K. Lee, and H. Choi, Opposite behavior of ultrafast dynamics of exciton shift and linewidth broadening in bilayer ReS<sub>2</sub>, *Phys. Rev. B* **103**, 014309 (2021).
- [40] C. H. Ho, P. C. Yen, Y. S. Huang, and K. K. Tiong, Photoreflectance study of the excitonic transitions of rhenium disulphide layer compounds, *Phys. Rev. B* **66**, 245207 (2002).
- [41] S. Das, S. Prasad, B. Chakraborty, B. Jariwala, S. Shradha, D. V. S. Muthu, A. Bhattacharya, U. V. Waghmare, and A. K. Sood, Doping controlled Fano resonance in bilayer 1T'-ReS<sub>2</sub>: Raman experiments and first-principles theoretical analysis, *Nanoscale* **13**, 1248 (2021).
- [42] C. H. Ho, Y. S. Huang, K. K. Tiong, and P. C. Liao, Absorption-edge anisotropy in ReS<sub>2</sub> and ReSe<sub>2</sub> layered semiconductors, *Phys. Rev. B* **58**, 16130 (1998).
- [43] H. Jang, C. R. Ryder, J. D. Wood, M. C. Hersam, and D. G. Cahill, 3D anisotropic thermal conductivity of exfoliated rhenium disulfide, *Adv. Mater.* **29**, 1700650 (2017).
- [44] C. Ruppert, A. Chernikov, H. M. Hill, A. F. Rigosi, and T. F. Heinz, The role of electronic and phononic excitation in the optical response of monolayer WS<sub>2</sub> after ultrafast excitation, *Nano Lett.* **17**, 644 (2017).
- [45] Z. Guo, Y. Wan, M. Yang, J. Snaider, K. Zhu, and L. Huang, Long-range hot-carrier transport in hybrid perovskites visualized by ultrafast microscopy, *Science* **356**, 59 (2017).
- [46] P. Schiettecatte, P. Geiregat, and Z. Hens, Ultrafast carrier dynamics in few-layer colloidal molybdenum disulfide probed by broadband transient absorption spectroscopy, *J. Phys. Chem. C* **123**, 10571 (2019).
- [47] S. Bae, S. Nah, D. Lee, M. Sajjad, N. Singh, K. M. Kang, S. Kim, G. J. Kim, J. Kim, H. Baik, *et al.*, Exciton-dominated ultrafast optical response in atomically thin PtSe<sub>2</sub>, *Small* **17**, 2103400 (2021).
- [48] E. J. Sie, A. Steinhoff, C. Gies, C. H. Lui, Q. Ma, M. Rösner, G. Schönhoff, F. Jahnke, T. O. Wehling, Y. H. Lee, *et al.*, Observation of exciton redshift-blueshift crossover in monolayer WS<sub>2</sub>, *Nano Lett.* **17**, 4210 (2017).
- [49] A. Chernikov, T. C. Berkelbach, H. M. Hill, A. Rigosi, Y. Li, O. B. Aslan, D. R. Reichman, M. S. Hybertsen, and T. F. Heinz, Exciton binding energy and nonhydrogenic Rydberg series in monolayer WS<sub>2</sub>, *Phys. Rev. Lett.* **113**, 076802 (2014).
- [50] L. Wang, S. Zhang, J. Huang, Y. Mao, N. Dong, X. Zhang, I. M. Kisllyakov, H. Wang, Z. Wang, C. Chen, *et al.*, Auger-type process in ultrathin ReS<sub>2</sub>, *Opt. Mater. Express* **10**, 1092 (2020).
- [51] Y. D. Glinka, R. Cai, J. Li, T. He, and X. W. Sun, Observing dynamic and static Rashba effects in a thin layer of 3D hybrid perovskite nanocrystals using transient absorption spectroscopy, *AIP Adv.* **10**, 105034 (2020).
- [52] V. R. Munirov and N. J. Fisch, Inverse bremsstrahlung current drive, *Phys. Rev. E* **96**, 053211 (2017).
- [53] S. Sim, M. Brahlek, N. Koirala, S. Cha, S. Oh, and H. Choi, Ultrafast terahertz dynamics of hot Dirac-electron surface scattering in the topological insulator Bi<sub>2</sub>Se<sub>3</sub>, *Phys. Rev. B* **89**, 165137 (2014).
- [54] H. J. Shin, J. M. Lee, S. Bae, W. H. Kim, and S. Sim, Metal-insulator transition and interfacial thermal transport in atomic layer deposited Ru nanofilms characterized by ultrafast terahertz spectroscopy, *Appl. Surf. Sci.* **563**, 150184 (2021).
- [55] Y. Aytac, M. Mittendorff, and T. E. Murphy, Probing the free-carrier absorption in multi-layer black phosphorus, *Appl. Phys. Lett.* **113**, 031108 (2018).
- [56] P. Y. Yu and M. Cardona, *Fundamentals of Semiconductors*, 3rd ed. (Springer, New York, 2005).
- [57] A. Laturia, M. L. van de Put, and W. G. Vandenberghe, Dielectric properties of hexagonal boron nitride and transition metal dichalcogenides: From monolayer to bulk, *NPJ 2D Mater. Appl.* **2**, 6 (2018).
- [58] J. L. Webb, L. S. Hart, D. Wolverson, C. Chen, J. Avila, and M. C. Asensio, Electronic band structure of ReS<sub>2</sub> by high-resolution angle-resolved photoemission spectroscopy, *Phys. Rev. B* **96**, 115205 (2017).
- [59] B. S. Kim, W. S. Kyung, J. D. Denlinger, C. Kim, and S. R. Park, Strong one-dimensional characteristics of hole-carriers in ReS<sub>2</sub> and ReSe<sub>2</sub>, *Sci. Rep.* **9**, 2730 (2019).
- [60] C. H. Ho, H. W. Lee, and C. C. Wu, Polarization sensitive behaviour of the band-edge transitions in ReS<sub>2</sub> and ReSe<sub>2</sub> layered semiconductors, *J. Phys.: Condens. Matter* **16**, 5937 (2004).
- [61] Y. Yang, D. P. Ostrowski, R. M. France, K. Zhu, J. van de Lagemaat, J. M. Luther, and M. C. Beard, Observation of a hot-phonon bottleneck in lead-iodide perovskites, *Nat. Photonics* **10**, 53 (2016).
- [62] Z. Nie, R. Long, L. Sun, C. C. Huang, J. Zhang, Q. Xiong, D. W. Hewak, Z. Shen, O. V. Prezhdo, and Z. H. Loh, Ultrafast carrier thermalization and cooling dynamics in few-layer MoS<sub>2</sub>, *ACS Nano* **8**, 10931 (2014).
- [63] S. Zhao, D. He, J. He, X. Zhang, L. Yi, Y. Wang, and H. Zhao, Probing excitons in transition metal dichalcogenides by Drude-like exciton intraband absorption, *Nanoscale* **10**, 9538 (2018).
- [64] K. Wang, J. Wang, J. Fan, M. Lotya, A. O'Neill, D. Fox, Y. Feng, X. Zhang, B. Jiang, Q. Zhao, *et al.*, Ultrafast saturable absorption of two-dimensional MoS<sub>2</sub> nanosheets, *ACS Nano* **7**, 9260 (2013).

- [65] R. D. Kekatpure and M. L. Brongersma, Quantification of free-carrier absorption in silicon nanocrystals with an optical microcavity, *Nano Lett.* **8**, 3787 (2008).
- [66] H. Peelaers, E. Kioupakis, and C. G. van de Walle, Fundamental limits on optical transparency of transparent conducting oxides: Free-carrier absorption in SnO<sub>2</sub>, *Appl. Phys. Lett.* **100**, 011914 (2012).
- [67] C. Xiang, W. Jin, D. Huang, M. A. Tran, J. Guo, Y. Wan, W. Xie, G. Kurczveil, A. M. Netherton, D. Liang, *et al.*, High-performance silicon photonics using heterogeneous integration, *IEEE J. Sel. Top. Quantum Electron.* **28**, 8200515 (2022).
- [68] Y. Kim, J. H. Han, D. Ahn, and S. Kim, Heterogeneously-integrated optical phase shifters for next-generation modulators and switches on a silicon photonics platform: A review, *Micromachines* **12**, 625 (2021).
- [69] M. Liu, X. Yin, E. Ulin-Avila, B. Geng, T. Zentgraf, L. Ju, F. Wang, and X. Zhang, A graphene-based broadband optical modulator, *Nature* **474**, 64 (2011).
- [70] I. Datta, S. H. Chae, G. R. Bhatt, M. A. Tadayon, B. Li, Y. Yu, C. Park, J. Park, L. Cao, D. N. Basov, *et al.*, Low-loss composite photonic platform based on 2D semiconductor monolayers, *Nat. Photonics* **14**, 256 (2020).
- [71] Y. T. Hu, M. Pantouvaki, S. Brems, I. Asselberghs, C. Huyghebaert, M. Geisler, C. Alessandri, R. Baets, P. Absil, D. Van Thourhout, *et al.*, in *2014 IEEE International Electron Devices Meeting*, San Francisco, CA, USA, (IEEE, 2014), p. 5.6.1.
- [72] B. J. Huang, C. T. Tsai, Y. H. Lin, C. H. Cheng, H. Y. Wang, Y. C. Chi, P. H. Chang, C. I. Wu, and G. R. Lin, SiGeC waveguide for all-optical data switching, *ACS Photonics* **5**, 2251 (2018).
- [73] Y. Kim, J. Fujikata, S. Takahashi, M. Takenaka, and S. Takagi, Demonstration of record-low injection-current variable optical attenuator based on strained SiGe with optimized lateral pin junction, *Opt. Express* **23**, 12354 (2015).
- [74] M. Takenaka, Y. Kim, J. Han, J. Kang, Y. Ikku, Y. Cheng, J. Park, M. Yoshida, S. Takashima, and S. Takagi, Heterogeneous CMOS photonics based on SiGe/Ge and III-V semiconductors integrated on Si platform, *IEEE J. Sel. Top. Quantum Electron.* **23**, 8200713 (2017).
- [75] J. Shim, J. Lim, D. M. Geum, J. B. You, H. Yoon, J. P. Kim, W. J. Baek, J. H. Han, and S. Kim, TiO<sub>x</sub>/Ti/TiO<sub>x</sub> tri-layer film-based waveguide bolometric detector for on-chip Si photonic sensor, *IEEE Trans. Electron Devices* **69**, 2151 (2022).
- [76] D. Lee, S. Y. Han, Y. Jeong, D. M. Nguyen, G. Yoon, J. Mun, J. Chae, J. H. Lee, J. G. Ok, G. Y. Jung, *et al.*, Polarization-sensitive tunable absorber in visible and near-infrared regimes, *Sci. Rep.* **8**, 12393 (2018).
- [77] H. Liu, Z. Li, Y. Yu, J. Lin, S. Liu, F. Pang, and T. Wang, Nonlinear optical properties of anisotropic two-dimensional layered materials for ultrafast photonics, *Nanophotonics* **9**, 1651 (2020).
- [78] W. Shen, C. Hu, J. Tao, J. Liu, S. Fan, Y. Wei, C. An, J. Chen, S. Wu, Y. Li, *et al.*, Resolving the optical anisotropy of low-symmetry 2D materials, *Nanoscale* **10**, 8329 (2018).
- [79] Z. Guo, H. Gu, M. Fang, B. Song, W. Wang, X. Chen, C. Zhang, H. Jiang, L. Wang, and S. Liu, Complete dielectric tensor and giant optical anisotropy in quasi-one-dimensional ZrTe<sub>5</sub>, *ACS Mater. Lett.* **3**, 525 (2021).
- [80] G. Kresse and D. Joubert, From ultrasoft pseudopotentials to the projector augmented-wave method, *Phys. Rev. B* **59**, 1758 (1999).
- [81] S. Grimme, J. Antony, S. Ehrlich, and H. Krieg, A consistent and accurate *ab initio* parametrization of density functional dispersion correction (DFT-D) for the 94 elements H-Pu, *J. Chem. Phys.* **132**, 154104 (2010).
- [82] A. Seidl, A. Görling, P. Vogl, J. A. Majewski, and M. Levy, Generalized Kohn-Sham schemes and the band-gap problem, *Phys. Rev. B* **53**, 3764 (1996).
- [83] M. Gehlmann, I. Aguilera, G. Bihlmayer, S. Nemšák, P. Nagler, P. Gospodarič, G. Zamborlini, M. Eschbach, V. Feyer, F. Kronast, *et al.*, Direct observation of the band gap transition in atomically thin ReS<sub>2</sub>, *Nano Lett.* **17**, 5187 (2017).
- [84] N. B. Mohamed, K. Shinokita, X. Wang, H. E. Lim, D. Tan, Y. Miyauchi, and K. Matsuda, Photoluminescence quantum yields for atomically thin-layered ReS<sub>2</sub>: Identification of indirect-bandgap semiconductors, *Appl. Phys. Lett.* **113**, 121112 (2018).
- [85] A. Dhara, D. Chakrabarty, P. Das, A. K. Pattanayak, S. Paul, S. Mukherjee, and S. Dhara, Additional excitonic features and momentum-dark states in ReS<sub>2</sub>, *Phys. Rev. B* **102**, 161404 (2020).
- [86] S. Bae and S. Sim, Anisotropic excitons in 2D rhenium dichalcogenides: A mini-review, *J. Korean Phys. Soc.* (2022).